remote sensing

MDPI

Article

Fine-scale Eddies Revealed by the Surface Water and Ocean Topography (SWOT) Mission

Zhibin Yang [1], Zhao Jing [1,2*], Xiaoming Zhai [3], Qinbiao Ni [4]

[1] Laoshan Laboratory, Qingdao 266237, China; zbyang1@qnlm.ac
[2] Physical Oceanography Laboratory, Ocean University of China, Qingdao 266100, China;
[3] Centre for Ocean and Atmospheric Sciences, School of Environmental Sciences, University of East Anglia, Norwich NR4 7TJ, United Kingdom; xiaoming.zhai@uea.ac.uk
[4] Southern Marine Science and Engineering Guangdong Laboratory (Zhuhai), Zhuhai 519000, China. niqinbiao@sml-zhuhai.cn

* Correspondence: jingzhao@ouc.edu.cn

Highlights

What are the main findings?

- Fine-scale eddies (radius < 30 km) show a pronounced winter peak in occurrence and amplitude, contrasting with the nearly seasonally invariant mesoscale eddy field.
- Cyclonic fine-scale eddies vastly outnumber anticyclonic ones and are stronger in amplitude, revealing a robust polarity asymmetry driven by frontogenesis and ageostrophic instabilities.

What are the implications of the main findings?

- The distinct seasonality and polarity dominance of fine-scale eddies lead to the hypothesis that their energy cascade and tracer transport cannot be simply extrapolated from mesoscale dynamics.
- The net ~7% enhancement of surface chlorophyll-a within eddy cores underscores the need to represent fine-scale eddies in next-generation ocean biogeochemical models.

Academic Editor: Firstname Lastname

Received: date
Revised: date
Accepted: date
Published: date

Citation: To be added by editorial staff during production.

Copyright: © 2025 by the authors. Submitted for possible open access publication under the terms and conditions of the Creative Commons Attribution (CC BY) license (https://creativecommons.org/licenses/by/4.0/).

Abstract: Utilizing two-dimensional sea level anomalies from the Surface Water and Ocean Topography (SWOT) wide-swath altimeter, we conduct a global census of fine-scale eddies (with equivalent radii < 30 km) that are beyond the resolution capacity of traditional altimeters. We find that these eddies are concentrated in regions with energetic mesoscale currents such as western boundary current extensions, the Antarctic Circumpolar Current and prominent interior frontal zones. While these eddies are smaller than classical mesoscale eddies (O(100) km), they exhibit dynamics distinct from the mesoscale, including a pronounced winter peak in occurrence frequency and a striking dominance of cyclonic over anticyclonic polarities. A global composite reveals a net enhancing effect of these fine-scale eddies on surface chlorophyll-a (approximately +7% within eddy cores relative to surrounding waters). Our findings shed light on the dynamical characteristics and surface chlorophyll-a signatures of fine-scale ocean eddies, necessitating their adequate representation in next-generation ocean models.

Keywords: SWOT; fine-scale eddies; altimeter; chlorophyll-a

1. Introduction

For decades, satellite altimetry has revolutionized our understanding of oceanic mesoscale eddies, which typically span tens to several hundreds of kilometres depending on latitude and regional dynamics. Global eddy censuses built from conventional nadir-altimeter data have mapped their ubiquitous distribution and quantified their roles in transporting heat and biogeochemical tracers [1-5]. However, this established view is fundamentally incomplete. The effective resolution of conventional along-track measurements (typically >100 km) and their multi-day revisit times act as a low-pass filter [6,7], obscuring a vast population of smaller, faster-evolving features at the submesoscale. Dynamically, mesoscale flows are characterized by small Rossby numbers ($Ro \ll 1$) indicating dominant geostrophic balance, whereas submesoscale motions exhibit order-one Rossby numbers ($Ro \sim 1$ or larger) and ageostrophic dynamics become important [8]. These fine-scale eddies are hypothesized to be critical agents in the energy cascade and vertical transport, mediating the transfer of energy and tracers from mesoscale flows and modulating climate-relevant processes such as carbon export and ocean heat uptake [9-12].

The classical tools for identifying and tracking ocean eddies—whether based on closed sea-level anomaly (SLA) contours [2,3], the Okubo–Weiss (OW) parameter [13,14], or the winding-angle method [15]—were all designed for, and applied to, products from conventional altimeters. Because the gridded altimetry fields on which they rely have an effective resolution of about 100 km, smaller eddies are systematically absent from the widely used mesoscale eddy datasets [3].

The Surface Water and Ocean Topography (SWOT) mission, carrying a Ka-band radar interferometer, provides two-dimensional SLA at an effective resolution of ~10 km over a wide swath, enabling the first systematic detection of fine-scale eddies on a global scale [16,17]. Since the launch and early data releases of SWOT, its capability to capture fine-scale eddy features has been demonstrated in a growing number of regional investigations. Individual fine-scale eddies and eddy trains have been identified in the Kuroshio Extension [18,19], the Western Pacific [20,21], the South China Sea [22] and the Mediterranean Sea [23]. Notably, all of these efforts remain restricted to specific regions, short time periods, or a small number of individual eddy snapshots. A systematic, global-scale census of fine-scale eddies directly from SWOT is still lacking.

To address this gap, we present a global census of fine-scale eddies based on SLA geometry using SWOT wide-swath altimetry. We adopt a geometric definition and identify 'fine-scale eddies' as those with equivalent radii < 30 km. A separate dynamical classification based on the Rossby number (Ro) shows that 78.6% of these geometrically defined eddies exhibit $Ro > 0.5$, indicating that the majority fall within the ageostrophic submesoscale regime, while the remainder ($Ro < 0.5$) represent the smaller end of the mesoscale spectrum (the $Ro = 0.5$ threshold is conservative; only ~1% of extratropical mesoscale eddies exceed $Ro = 0.1$ [3]). To distinguish their dynamics from the well-characterized mesoscale field, we systematically contrast this fine-scale population against a parallel mesoscale eddy census derived from conventional altimetry. We analyse global distribution, seasonal dynamics, polarity asymmetry, and surface chlorophyll-a (Chl-a) signatures. Our results reveal a fine-scale eddy field that is dynamically distinct from the mesoscale, featuring a pronounced winter peak in activity and a striking dominance of cyclonic eddies (CEs) over anticyclonic eddies (AEs), and a net enhancing effect on surface Chl-a.

2. Data

2.1. SWOT data

We employ the release (version 2.0.1) of the Level-3 SWOT product, which features a 2-km posting grid. This product has undergone rigorous processing to remove systematic errors and has been extensively validated globally [24]. Specifically, we use the "filtered" SLA variable provided in this dataset. This variable is derived using a U-Net–based convolutional neural network filtering method, which has been shown to effectively reduce observational noise while preserving the balanced geophysical signal [25]. The U-Net achieves a variance reduction factor of 44 (~16 dB) and a root-mean-square error of only 2 mm, and it accurately reproduces the power spectral density of SSH down to 10–20 km wavelengths as well as its first and second spatial derivatives. These characteristics indicate that the filtering effectively suppresses random noise without significantly attenuating the amplitudes or distorting the gradients of the small-scale features that are critical for fine-scale eddy detection. The resulting effective resolution of the filtered SLA field is approximately 10 km. We analyze SWOT data covering the period from April 1, 2023, to September 30, 2025. This period encompasses the initial "1-day fast-sampling" (approximately the first three months) and the subsequent standard 21-day repeat “science phase” orbit. During the ‘1-day fast-sampling’ phase (approximately the first three months), SWOT operated on a 1-day repeat orbit, providing high-frequency observations but with limited spatial coverage between 78°S and 78°N. In the subsequent science phase, the satellite operates on a 21-day exact repeat orbit.

2.2. CMEMS data

For comparative analysis with mesoscale eddies, we complement the SWOT data with a gridded Level-4 SLA data from the Copernicus Marine Service (hereafter referred to as CMEMS; Product ID: SEALEVEL_GLO_PHY_L4_MY_008_047), with a spatial resolution of 0.125°×0.125°. This product merges along-track measurements from multiple altimeter missions using optimal interpolation, providing a continuous and consistent global field.

2.3. MODIS data

We use Level-2 sea surface temperature (SST) and Chl-a data from the MODIS-Aqua and MODIS-Terra platforms for the period April 2023–September 2025, coincident with the SWOT altimetry record. The specific products are MODISA_L2_SST and MODIST_L2_SST for SST, and MODISA_L2_OC and MODIST_L2_OC for Chl-a (version R2022.0, NASA Ocean Biology Processing Group). These Level-2 data provide geophysical variables along the orbital track at a spatial resolution of approximately 1 km, which is essential for resolving fine-scale structures.

Only high-quality pixels are retained for analysis. We mask any pixel whose Level-2 quality flag indicates ATMFAIL, LAND, HIGLINT, HILT, HISATZEN, STRAYLIGHT, CLDICE, HISOLZEN, or CHLFAIL (corresponding bitmask values: 1, 2, 8, 16, 64, 256, 512, 4096, 16384). This filtering ensures that only cloud-free, well-navigated, and atmospherically corrected observations are used.

When an eddy is simultaneously matched with valid observations from both Aqua and Terra within the ±4-hour collocation window, we retain the platform that yields the larger number of unmasked, high-quality pixels inside the eddy core. No cross-platform averaging is performed, in order to avoid mixing different overpass times and viewing geometries.

To construct a reference climatology, we average the Level-4 monthly Chl-a products (MODIS-Aqua, 4 km resolution) over the period 2003–2024.

2.4. World Ocean Atlas data

The climatological buoyancy frequency is computed from the World Ocean Atlas 2018 (WOA18) monthly temperature and salinity climatology (1995–2004) on a 0.25° × 0.25° horizontal grid with 102 vertical levels. The mixed layer depth climatology is also from the corresponding WOA18 mixed layer depth product.

3. Methods

3.1. Eddy identification method

Fine-scale and mesoscale eddies are identified from their respective SLA fields using an automated, geometry-based algorithm. This approach follows and extends the foundational frameworks established for mesoscale eddy detection [3,26]. For a given two-dimensional SLA field (from either SWOT or CMEMS), closed contours are first derived at an interval of 0.2 cm for fine-scale eddies and 1 cm for mesoscale eddies. Within each nest of contours, the SLA extremum of the innermost loop is designated as the eddy center. The eddy's edge is defined by the outermost closed contour that contains this single center. The amplitude is calculated as the absolute SLA difference between the center and this edge. The equivalent radius R is computed as the radius of a circle whose area matches the area enclosed by the edge. To minimize spurious detections associated with shallow coastal processes and complex bathymetry, we retain only SLA observations over water depths greater than 200 m.

For fine-scale eddies from SWOT, pixels with quality flag other than 0 (good) or 18 (ocean_unsure) are masked before eddy identification. A primary filter retains only initial detections with equivalent radius>5 km and amplitude>2 cm. A sensitivity analysis using larger minimum radius thresholds of 7.5, 10, and 15 km confirms that the main statistical properties of the eddy field—including the seasonal amplitude cycle and the polarity asymmetry—are insensitive to this choice. To ensure the identified edge is not an artifact of incomplete coverage, we implement a verification procedure (Figure 1). For the initially detected outermost contour, we search in its immediate vicinity for the nearest contours at SLA values 0.5 cm higher and 0.5 cm lower. A sensitivity test using a smaller search increment of 0.2 cm yields nearly identical eddy populations and does not alter the main conclusions. These three contours are resampled in a polar coordinate system centered on the eddy at 10° intervals. For each angle θ, the radial distances from the eddy center to the inner contour ($R_{\theta,\mathrm{inner}}$), the initial edge ($R_\theta$), and the outer contour ($R_{\theta,\mathrm{outer}}$) are calculated. The radial gaps are defined as $dR_{\theta,\mathrm{inner}} = R_\theta - R_{\theta,\mathrm{inner}}$ and $dR_{\theta,\mathrm{outer}} = R_{\theta,\mathrm{outer}} - R_\theta$. The eddy candidate is rejected if the maximum ratio $dR_{\theta,\mathrm{outer}} / dR_{\theta,\mathrm{inner}} < 2$ and mean ratio<1.5. While varying the thresholds (e.g., the maximum ratio <1.5 and mean ratio<1.25) altered the total number of eddies identified (57,363 *vs*. the original 39,997 within ±20°–60° latitudes for October 2023–September 2025), our main conclusions regarding the distinct seasonal cycle and polarity asymmetry of fine-scale eddies remained unchanged. Figure 1a shows an example of detected eddies from SWOT. In this example, four eddies are labeled A–D. Eddies A, C, and D are cyclonic, while Eddy B is anticyclonic. Eddy C is rejected because the radial distances of its outermost closed contour and the inner contour are too similar to pass the contour verification criterion. Additionally, at approximately 145.7° E, 24.6° N, a large CE is initially identified as three separate eddies, as the closed-contour algorithm allows only one center per contour nest; all three are subsequently discarded because their amplitudes are below the 2 cm threshold. All other closed SLA contours that are not identified as eddies because their amplitudes are below the 2 cm threshold or equivalent radii below 5 km are likewise marked by red squares.

For mesoscale eddies from CMEMS, the identification process follows the same geometric algorithm but omits the outermost contour validation.

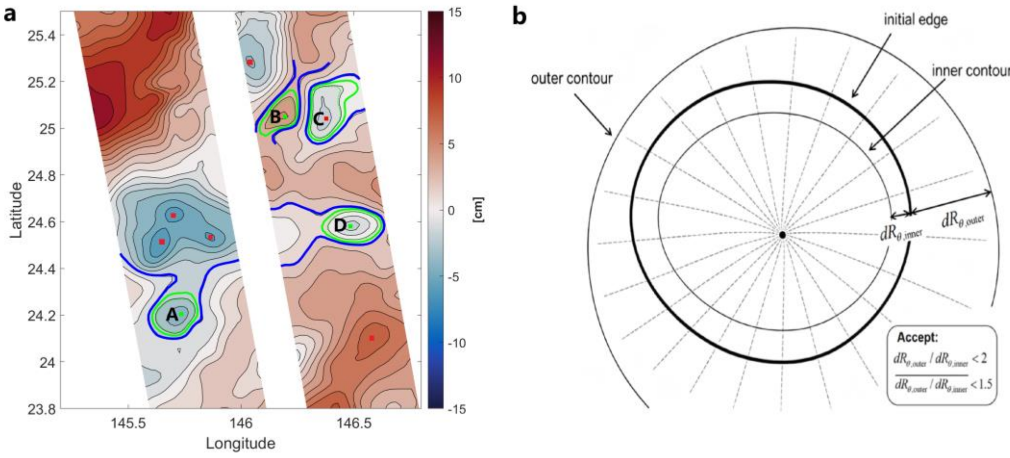

Figure 1. Example of fine-scale eddy identification from SWOT. (a) Four eddies (A–D) are detected, with eddies A, C and D being cyclonic and eddy B anticyclonic. The green solid line denotes the initially identified eddy edge, the green dashed line the inner contour, and the blue solid line the outer contour used in the verification step. Eddy C is rejected (its center is marked by a red square) because the radial distances of its outer and inner contours are too similar to pass the contour verification criterion; the centers of the remaining three eddies that passed validation are marked by green squares. All other closed SLA contours that are not identified as eddies because their amplitudes are below the 2 cm threshold or equivalent radii below 5 km are likewise marked by red squares. Color shading represents the SLA on February 1, 2024 (cycle 10) with 1 cm interval contours. (b) Schematic of the outer-contour validation criterion. Radial gaps are measured at 10° polar intervals. The eddy is accepted only if the maximum and mean ratios of $dR_{\theta,\text{outer}} / dR_{\theta,\text{inner}} < 2$ and mean ratio<1.5.

3.2. Eddy validation framework

We implemented a temporal persistence criterion to ascertain that the fine-scale eddies identified from SWOT data represent vortices rather than transient noise or wave-like features: during SWOT's initial "1-day fast-sampling" phase (April-June 2023), the persistence of eddies is assessed. For a given "primary" eddy detection, a successful match is declared if another eddy of the same polarity (cyclonic/anticyclonic) with an SLA amplitude>2 cm is found within a ±48-hour window and within a 20 km radius of the primary eddy's center. The matched feature is required to show coherent structure but do not need to satisfy all strict identification filters (e.g., possessing an outermost closed contour).

3.3. OW parameter

To complement the geometry-based eddy identification with an independent dynamical assessment, we compute additional diagnostics for each detected eddy. The OW parameter is defined as:

$$\mathrm{OW} = s_n^2 + s_s^2 - \omega^2, \quad (1)$$

where $s_n = \partial u / \partial x - \partial v / \partial y$ is the normal strain rate, $s_s = \partial v / \partial x + \partial u / \partial y$ is the shear strain rate, and $\omega = \partial v / \partial x - \partial u / \partial y$ is the relative vorticity. u, v are the zonal and meridional geostrophic velocity components, respectively. Pixels with quality flag other than 0 (good) or 18 (ocean_unsure) are masked before computing the OW parameter.

We define a relative threshold $\mathrm{W}_0 = -0.2\sigma_{\mathrm{W}}$, where σ_{W} is the standard deviation of the local OW distribution (computed within 0.2°×0.2° bins over the two full years from

October 2023 to September 2025) [27]. A sensitivity test using a larger 1°×1° bin yields a nearly identical σ_W distribution and a comparable fraction of vorticity-dominated eddies.

The Rossby number is computed as:

$$\mathrm{Ro} = |\omega / f|, \quad (2)$$

where f is the local Coriolis parameter.

3.4. Mixed layer instability scale

To provide a dynamical context for the observed fine-scale eddy radii, we estimate the mixed layer instability scale:

$$Ld = NH/f, \quad (3)$$

where N is the buoyancy frequency averaged in the mixed layer and H is the mixed layer depth.

4. Results

4.1. Validation of Fine-scale Eddies

To ensure that the eddies identified from SWOT SLA represent robust physical features rather than transient noise, we applied an eddy validation framework, which assesses their robustness based on their temporal persistence. The probability of a fine-scale eddy meeting the validation criterion exhibits a strong latitudinal dependence (Figure 2). The probabilities for temporal persistence are low in the tropics (within ±20°) and increase poleward. Within the ±20°–60° latitude band, the validation probabilities are 67.9% for temporal persistence (from a total of 4,640 eddies during April-June 2023). When the matching window is tightened to ±24 h, the overall temporal persistence rate decreases to 57.4%, but the latitudinal dependence remains nearly identical to that shown in Figure 2.

Given that the 1-day fast-sampling phase provided only limited spatial coverage rather than global coverage (Figure 2a), and that temporal persistence validation is feasible only during this phase, it is important to assess whether combining eddy detections from the fast-sampling and 21-day science phases introduces systematic biases, given that the 21-day phase provides global coverage and substantially extends the geographic sampling of eddies. To this end, we compared the fine-scale eddy populations identified during the same calendar months (April–June) in three different years: the 2023 fast-sampling phase and the 2024 and 2025 science phases. The probability density functions (PDFs) of eddy amplitude and equivalent radius show no substantial differences across the three years (Figure 3), indicating that the sampling mode exerts a negligible systematic effect on the main statistical properties of the detected eddy field.

In addition to the probability distributions, we examined whether the pronounced polarity asymmetry in eddy amplitude—a defining characteristic of the fine-scale eddy field (see Section 4.3)—is consistently represented across phases (Figure 4). As an initial test, we focus on the fast-sampling period (April–June 2023). During this period, CEs are systematically stronger than AEs: 34.9% of CEs detected in April–June 2023 have amplitudes exceeding 3 cm, compared to only 23.3% of AEs. When the analysis is restricted to the temporally validated eddies, the contrast is equally evident (39.5% for CEs *vs*. 25.6% for AEs). This close agreement suggests that the non-validated detections share the same polarity-dependent amplitude skewness as the validated population, and thus likely contain a substantial fraction of genuine fine-scale eddies, although the presence of some transient or noisy features cannot be excluded. Although this comparison is limited to a single season, these percentages closely match those obtained from the full two-year science-phase census (32.1% for CEs *vs*. 22.6% for AEs; Section 4.3), and the seasonality analysis that follows (Section 4.2) confirms that the amplitude asymmetry persists throughout the year. Together with the cross-year agreement in the amplitude and radius (Figure 3; Figure 4) and the 67.9% temporal persistence rate, these results justify combining eddies identified from both phases in all subsequent analyses.

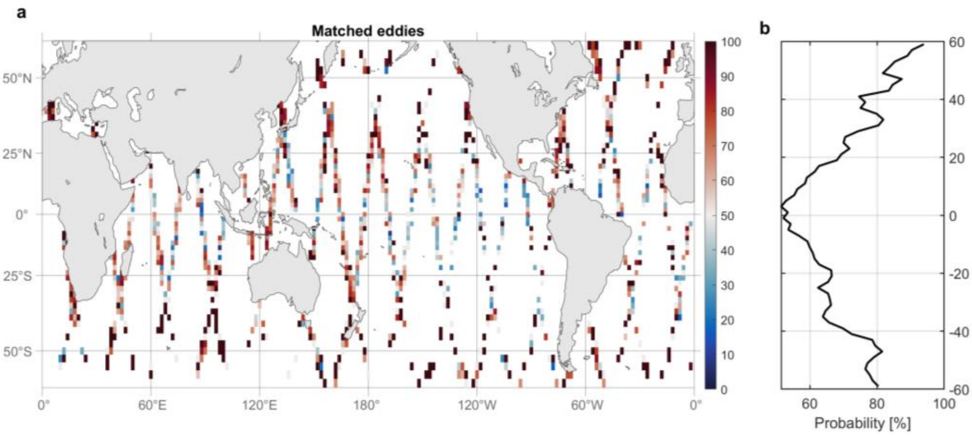

Figure 2. Temporal persistence validation of fine-scale eddies during the "1-day fast-sampling" phase. (a) Spatial distribution of the probability that a detected eddy is successfully matched with another eddy of the same polarity within ±48 h and 20 km. (b) Zonal-mean probability of meeting the temporal persistence criterion. Analysis is restricted to the fast-sampling period (April–June 2023) when daily revisit enables tracking.

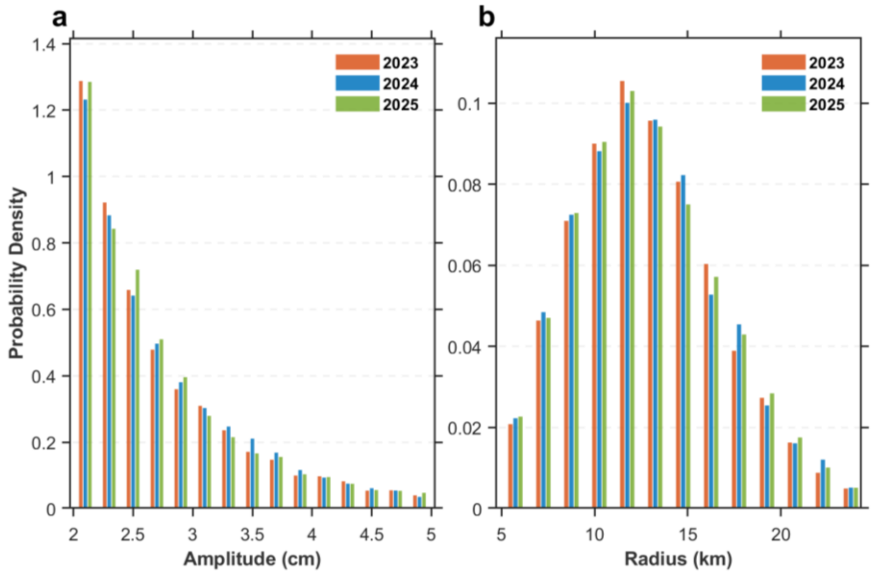

Figure 3. Comparison of eddy amplitude and radius distributions across different sampling phases. PDFs of (a) eddy amplitude and (b) equivalent radius for eddies detected during April–June in 2023 ("1-day fast-sampling" phase), 2024, and 2025 (21-day science phases).

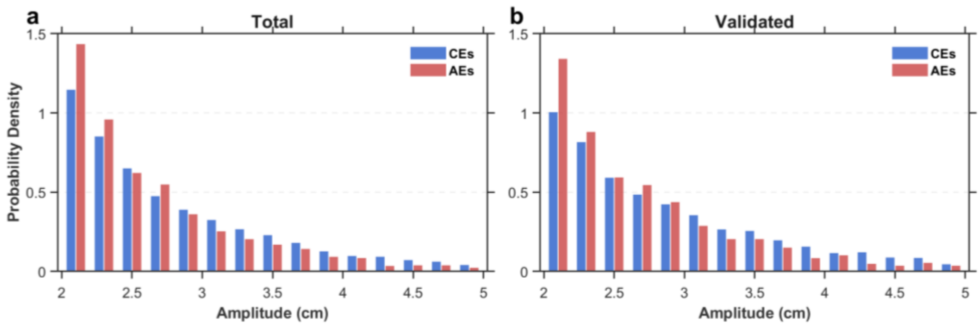

Figure 4. Polarity asymmetry in eddy amplitude during the "1-day fast-sampling" phase. PDFs of amplitude for (a) all detected eddies and (b) only temporally validated eddies. Blue and red bars denote CEs and AEs, respectively. Data are from the ±20°–60° latitude band during April–June 2023.

4.2. Seasonal Characteristics of Fine-scale Eddies

We present the statistical and geographical characteristics of fine-scale eddies identified over two full years (October 2023 – September 2025). Within the ±20°–60° latitude band, a total of 39,997 eddies are identified. Their occurrence frequency exhibits a pronounced seasonal cycle, characterized by a distinct winter (defined as December–May in the Northern Hemisphere and June–November in the Southern Hemisphere) peak and summer minimum. Specifically, 25,128 eddies are detected during local winter, compared to only 14,869 during local summer (Figure 5a). Normalising the eddy counts by the monthly effective observed area of the SWOT data leaves the seasonal cycle essentially unchanged. In contrast, the monthly counts of mesoscale eddies derived from CMEMS data show no discernible seasonal pattern, with much weaker month-to-month variation (Figure 5b), highlighting the unique seasonality inherent to fine-scale dynamical processes.

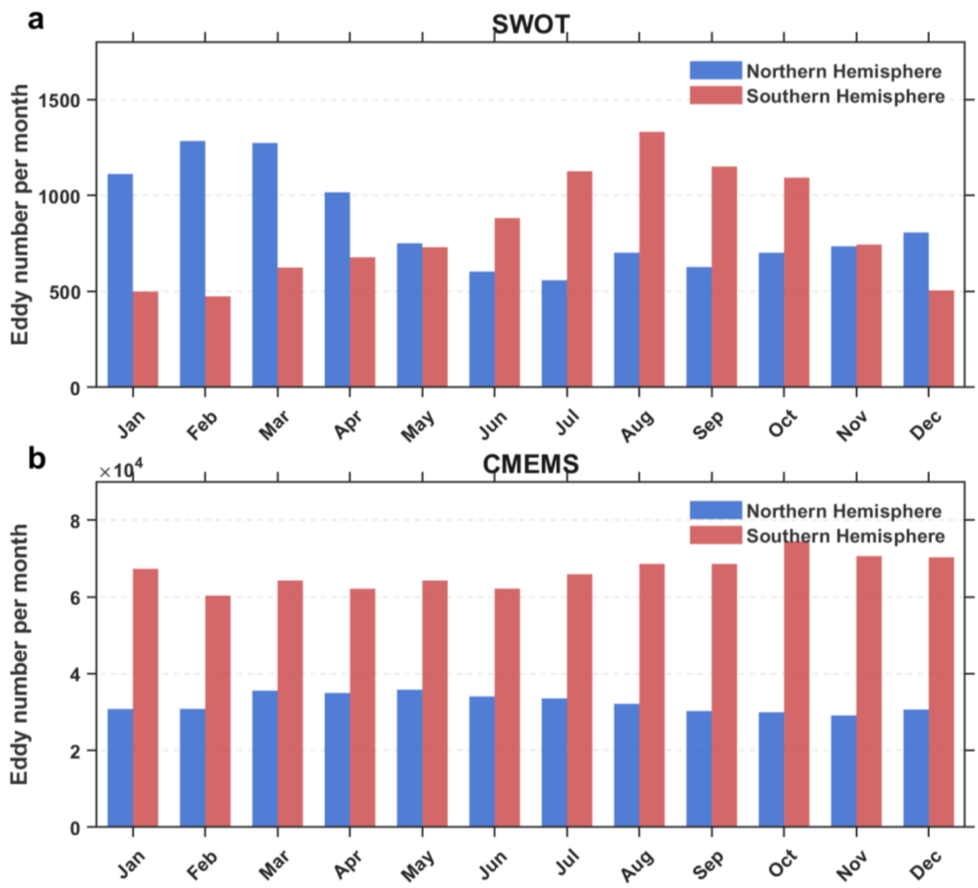

Figure 5. Seasonal contrast in monthly eddy counts. (a) Monthly fine-scale eddy number distribution from SWOT. (b) Same as (a), but for mesoscale eddies from CMEMS. Blue and red bars denote the Northern and Southern Hemisphere, respectively.

Spatially, fine-scale eddies are not uniformly distributed but are strongly concentrated in regions with energetic mesoscale currents (Figures 6a–d), such as western boundary current extensions, the Antarctic Circumpolar Current and the prominent interior frontal zones (e.g., the North Pacific Subtropical Countercurrent). These identified hotspots suggest fine-scale eddies may play a significant role in regional energy cascades and tracer transport [28-30]. Consistent with the spatial distribution of eddy numbers, regions of large amplitude generally coincide with areas of high eddy concentration (Figures 6e-h). The radius distribution of fine-scale eddies exhibits a latitudinal dependence, with smaller radii at higher latitudes and larger radii at lower latitudes, consistent with the scaling characteristics of fine-scale baroclinic instability (Figures 6i-l) [31].

The amplitude and radius statistics reveal distinct seasonal behaviours when examined through their PDFs (Figure 7). The amplitude shows a clear wintertime enhancement: 31.8% (95% confidence intervals = [31.3%, 32.4%]) of wintertime eddies have amplitudes exceeding 3 cm, compared to only 25.8% (95% confidence intervals = [25.1%, 26.5%]) in summer (Figure 7a). In contrast, mesoscale eddies from CMEMS display a much weaker seasonal contrast in amplitude (Figure 7c). We find no significant seasonal cycle in the eddy radius; the radius PDFs for fine-scale eddies show little difference between seasons (Figure 7b), and mesoscale eddy radii are similarly seasonally invariant (Figure 7d). It is important to note that the detection of eddy radius is subject to an observational limitation inherent to SWOT, due to both the instrument's swath width (one swath is approximately 60 km wide) and our identification criteria, which require an eddy to be fully contained within a single pass. When standard three-month seasons are used (e.g., JFM *vs.* JAS), the seasonal amplitude and radius PDFs are nearly identical to those in Figure 7.

We further examine the combined influence of season and polarity on eddy amplitude by comparing the proportions of eddies with amplitudes exceeding 3 cm across four categories: winter CEs, winter AEs, summer CEs, and summer AEs. CEs consistently dominate over AEs in both seasons: in winter, 34.6% (95% confidence intervals = [34.0%, 35.3%]) of CEs exceed 3 cm versus 22.6% (95% confidence intervals = [21.6%, 23.7%]) of AEs; in summer, the corresponding proportions are 28.4% (95% confidence intervals = [27.5%, 29.3%]) and 21.2% (95% confidence intervals = [20.1%, 22.3%]), respectively. The non-overlapping confidence intervals confirm that the cyclonic-anticyclonic amplitude asymmetry is statistically significant in both seasons. Additionally, a wintertime enhancement is evident for both polarities, but it is more pronounced for CEs.

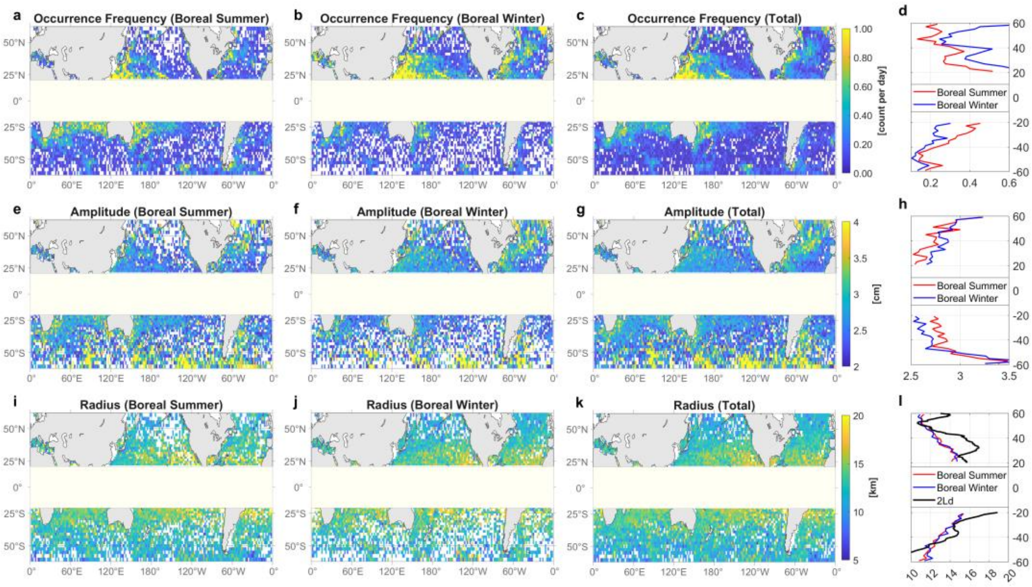

Figure 6. Seasonal characteristics of Fine-scale eddies. Geographical distribution of fine-scale eddy occurrence frequency for (a) boreal summer, (b) boreal winter and (c) total eddies within 2°×2° grid. (d) Zonal-mean eddy occurrence frequency over the study period (October 2023–September 2025). White areas in (a–c) denote regions without eddy detections. Red and blue lines in (d) denote boreal summer and boreal winter, respectively. (e–h) and (i–l) are the same as (a–d) but for eddy amplitude and equivalent radius, respectively. The black line in panel (l) indicates twice the mixed-layer instability scale.

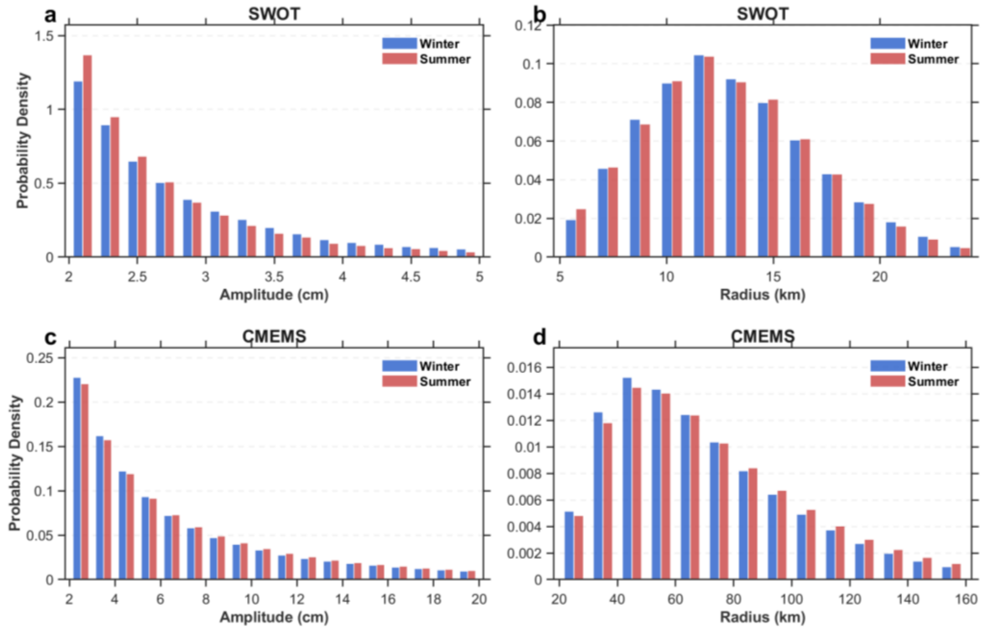

Figure 7. Seasonal distributions of eddy amplitude and radius. PDFs of (a) amplitude and (b) equivalent radius for fine-scale eddies identified from SWOT. (c-d) Same as (a-b), but for mesoscale eddies from CMEMS. Data are from the ±20°–60° latitude band over the study period (October 2023–September 2025). Blue and red bars denote local winter and local summer, respectively.

4.3. Polarity Characteristics of Fine-scale Eddies

A striking polarity asymmetry is evident in the spatial distribution of eddy number (Figures 8a-c). CEs vastly outnumber their AE counterparts, with 28,702 CEs identified compared to only 11,295 AEs. Spatially, CEs are widely distributed, though their concentration is highest in regions with energetic mesoscale currents and prominent interior frontal zones. In contrast, AEs exhibit a much sparser and more confined distribution. They are primarily found within intense western boundary currents and frontal zones, with only sparse occurrences elsewhere. The global dominance of CEs is consistent across latitudes, as shown in the zonal-mean result (Figure 8c).

For both polarities, regions of large eddy amplitude correspond to areas of high eddy concentration (Figures 8d-f). This amplitude polarity difference is even larger in regions with large eddy amplitude (e.g., the western boundary current extensions). Separating these regions based on annual mean amplitude, within these intense regions (where annual mean amplitude > 3 cm), the average amplitude for CEs is 3.62 cm (standard deviation = 1.96 cm, sample size = 7922), compared to 2.89 cm (standard deviation = 1.00 cm, sample size = 2352) for AEs. The mean amplitude difference is 0.73 cm (95% confidence interval: [0.67, 0.79] cm). In other regions, the amplitude of CEs is only slightly enhanced (2.7 cm for CEs *vs*. 2.6 cm for AEs).

The radius distributions of CEs and AEs show no fundamental difference in their latitudinal structure, both following the expected scaling with the baroclinic deformation radius (larger at low latitudes, smaller at high latitudes; Figures 8g-i) [31].

The PDFs of amplitude and radius further quantify these asymmetries (Figure 9). CEs are, on average, markedly stronger than AEs: 32.6% (95% confidence intervals = [32.0%, 33.1%]) of CEs have amplitudes exceeding 3 cm, whereas only 21.9% (95% confidence intervals = [21.2%, 22.7%]) of AEs reach this threshold (Figure 9a). A similar, though far less pronounced, polarity bias also exists for mesoscale eddies from CMEMS (Figure 9c). The radius PDFs reveal a subtle difference for smaller eddies (Figure 9b). For radii below 15 km, AEs tend to be slightly smaller, while CEs are associated with a broader distribution towards larger radii within this range, consistent with their stronger amplitudes. For radii greater than 15 km, the PDFs for the two polarities are similar. This pattern may be also influenced by observational limitations related to SWOT's swath width and our detection criteria. In contrast, for mesoscale eddies from CMEMS, the radius distribution shows a weak tendency, with AEs being slightly larger than CEs on average (Figure 9d).

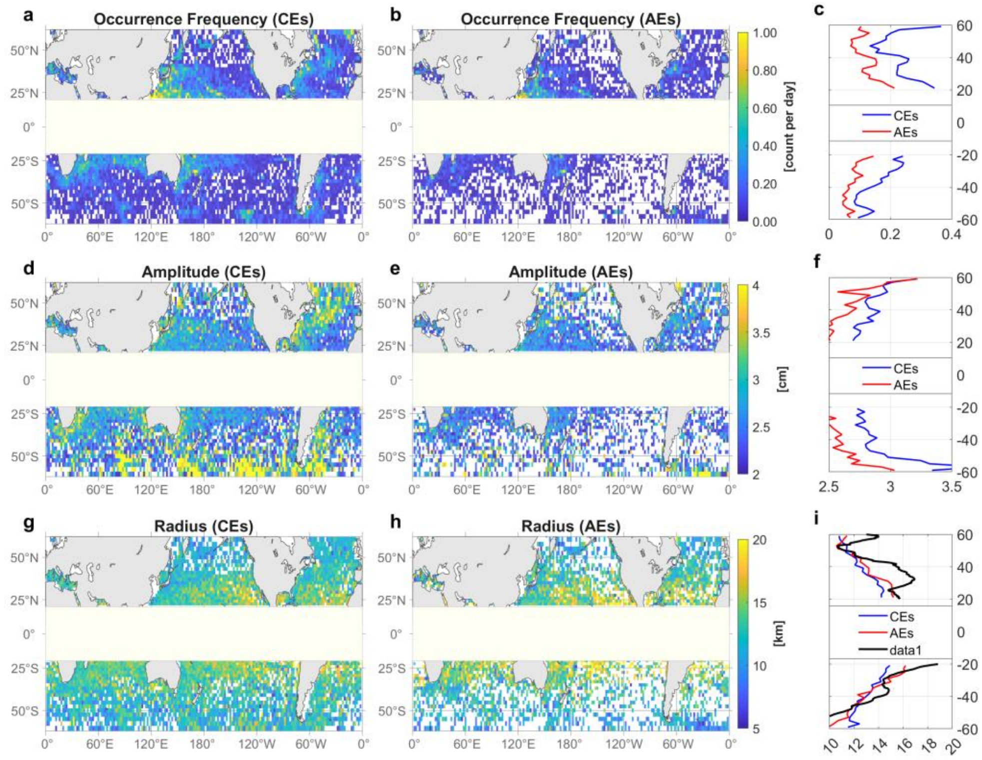

Figure 8. Polarity asymmetry of fine-scale eddies. Geographical distribution of fine-scale eddy occurrence frequency for (a) CEs and (b) AEs within 2°×2° grid. (c) Zonal-mean eddy occurrence frequency over the study period (October 2023–September 2025). White areas in (a-b) indicate regions with no eddy detections. Blue and red lines in (c) denote CEs and AEs, respectively. (d–f) and (g–i) are the same as (a–c) but for eddy amplitude and equivalent radius, respectively. The black line in panel (i) indicates twice the mixed-layer instability scale.

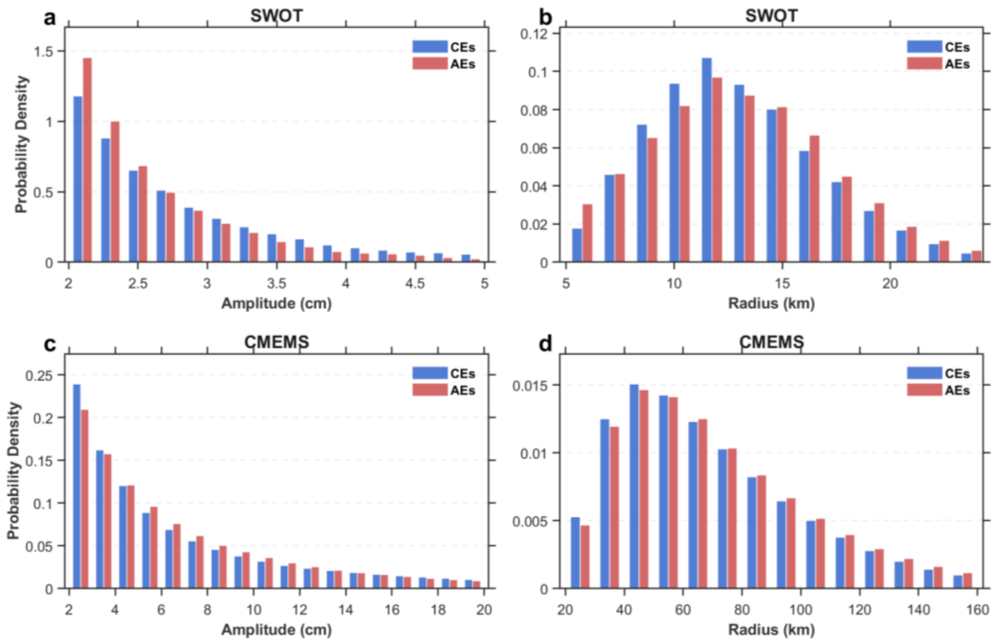

Figure 9. Polarity dependence of eddy amplitude and radius. PDFs of (a) amplitude and (b) equivalent radius for fine-scale eddies identified from SWOT. (c-d) Same as (a-b), but for mesoscale eddies from CMEMS. Data are from the ±20°–60° latitude band over the study period (October 2023–September 2025). Blue and red bars denote CEs and AEs, respectively.

4.4. Biogeochemical Signature of Fine-scale Eddies

Mesoscale eddies are classically expected to exhibit a canonical physical and biogeochemical signature: CEs are typically associated with cold SST and elevated surface Chl-a due to upwelling, while AEs are associated with warm SST and depressed Chl-a due to downwelling. However, this relationship does not hold universally. Previous studies have documented anomalous cases such as warm-core cyclones and cold-core anticyclones, although such cases account for only about 20% of global eddies [32].

To characterize the physical and biogeochemical signatures of fine-scale eddies, we collocate MODIS Level-2 SST and Chl-a data with each SWOT eddy. Following the classical mesoscale paradigm, we define an eddy as exhibiting a "normal" SST (or Chl-a) polarity if the interior anomaly is consistent with its dynamical polarity: cold SST/elevated Chl-a for CEs, and warm SST/depressed Chl-a for AEs. It should be noted that this definition is adopted solely as a mesoscale-based reference to characterize the observed signatures, rather than an a priori assumption that fine-scale eddies must conform to the canonical relationship [32,33]. Specifically, MODIS data are matched to each SWOT eddy within a ±4-hour window. For Chl-a, concentrations are first $\log_{10}$-transformed to approximate a normal distribution. To obtain a clean background signal, background pixels (2–3R from the eddy center) falling outside the [Q1 − 2×IQR, Q3 + 2×IQR] range of the interior (within 1R) values are excluded as extreme outliers, where Q1 and Q3 are the first and third quartiles, and IQR = Q3 − Q1 is the interquartile range. A Wilcoxon rank-sum test is then applied to compare the distributions of interior versus background pixels. We use the Wilcoxon test because SST and Chl-a distributions within eddy interiors and surrounding waters often deviate from normality, and the test is robust to such departures as well as to outliers originating from residual cloud contamination or submesoscale filaments. An eddy is considered to exhibit a normal SST (or Chl-a) polarity if the test indicates a statistically significant difference ($p < 0.1$) in the direction consistent with its dynamical polarity. A minimum of 30 valid pixels is required for each group, as this ensures the asymptotic normal approximation of the test statistic is reliable even in the presence of tied values.

Applying this analysis to fine-scale eddies within ±20°–60° latitude, we find that a clear majority (63.4%) exhibit the expected SST anomaly aligned with their dynamical polarity, consistent with the mesoscale paradigm. In contrast, the surface Chl-a response shows no such polarity-based relationship: only 48.3% of eddies exhibit the normal Chl-a polarity, a fraction indistinguishable from randomness. In fact, a substantial proportion (42.2%) of eddies show an opposite Chl-a signal. The remaining 9.5% of eddies show no statistically significant Chl-a polarity ($0.1 < p < 0.9$). Spatially, the distribution of eddies with a normal SST polarity follows a relatively regular pattern, predominantly concentrated outside ±20° latitude (Figure 10a), whereas the distribution of eddies with a normal Chl-a polarity is more scattered and irregular, with proportions consistently around 50% across most regions (Figure 10b).

This decoupling between SST and Chl-a signatures can be attributed to the short lifespans of fine-scale eddies, combined with the differing response timescales of physical versus biological processes. The SST field, which behaves like a near-passive tracer of the dynamical core, adjusts rapidly to vertical displacements induced by the eddy's geostrophic flow and ageostrophic frontal circulations, thereby more easily retaining a coherent polarity signal. In contrast, Chl-a concentration is the product of slower, nonlinear biogeochemical processes involving nutrient upwelling, phytoplankton growth, grazing, and loss. This integrated biological response may lag behind the eddy's dynamical evolution, such that the probability of observing a normal Chl-a signature is ~50%, indistinguishable from randomness.

Although the Chl-a signature in a single eddy is heterogeneous, a global composite analysis reveals that fine-scale eddies exert a net enhancing effect on surface Chl-a (Figure 11). Positive Chl-a anomalies are consistently concentrated around eddy centers, with the strength of enhancement varying by regime: weaker in Chl-a oligotrophic regions (monthly climatological Chl-a < 0.1 mg/m^3) and stronger in Chl-a productive zones. Globally, this yields a mean increase in surface Chl-a concentration of 3.81% within eddy cores (0–1R) relative to the surrounding waters (95% bootstrap confidence interval: [2.68%, 5.03%]). The spatial composite (Figure 11f) shows a peak enhancement of ~7% at the eddy center.

The observed net enhancement of surface Chl-a can be primarily attributed to a fundamental asymmetry in the vertical nutrient gradient—nutrient concentrations typically increase with depth, reaching high levels below the nutricline. Although fine-scale dynamics can generate strong vertical velocities in both directions, the strong background nutrient gradient ensures that, on average, upwelling effectively transports nutrients into the euphotic layer while downwelling removes nutrient-depleted water from it [33]. This creates an inherent biogeochemical bias favoring fertilization over dilution. Furthermore, this intrinsic asymmetry can be amplified by mixed-layer restratification associated with fine-scale flows [34], which helps to confine upwelled nutrients in the surface layer. The underlying mechanism is supported by the statistical distribution of the Chl-a response (Figure 12). Although the number of eddies associated with Chl-a increase and decrease is comparable (4,513 *vs*. 4,730), the PDF of locally normalized Chl-a anomalies is skewed, with strong enhancement events (e.g., >10%) occurring more frequently than comparable reduction events (25.7% *vs*. 18.2%), thereby generating the net enhanced signal.

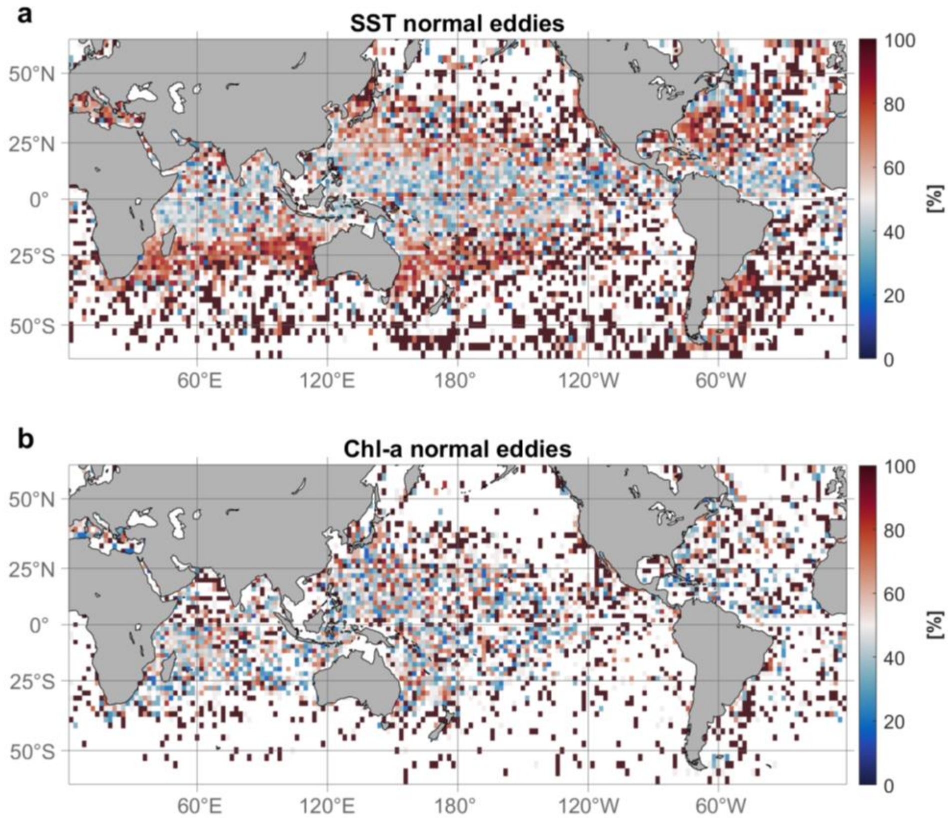

Figure 10. Spatial distributions of fine-scale eddies exhibiting normal polarity in SST and surface Chl-a. (a) The proportion of eddies displaying an SST anomaly aligned with their dynamical polarity within 2°×2° grid. (b) Same as (a), but for Chl-a anomaly.

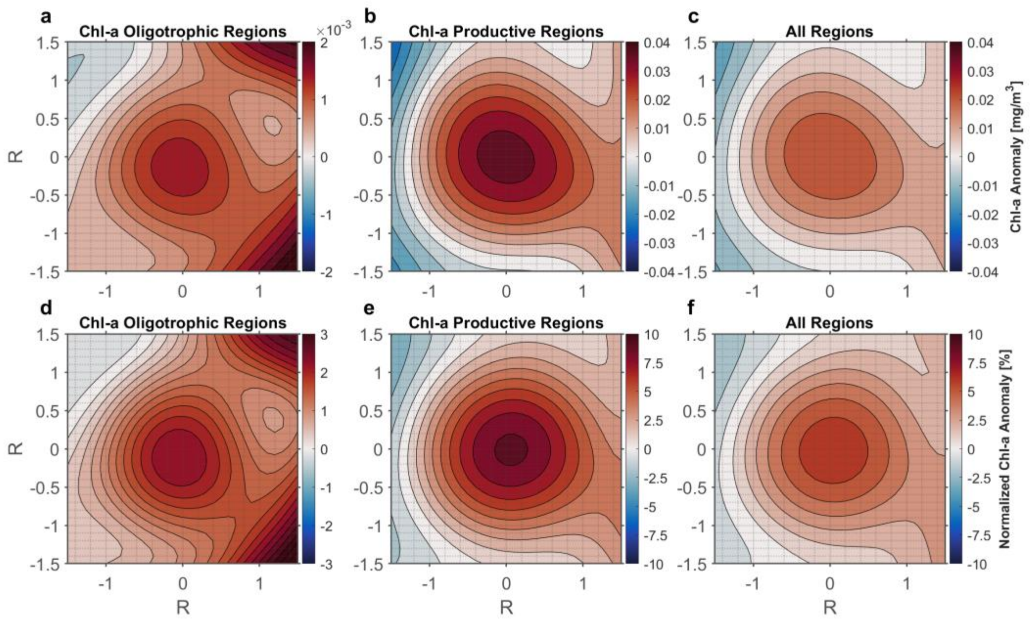

Figure 11. Composite surface Chl-a anomalies associated with fine-scale eddies. Absolute Chl-a anomaly composites for (a) Chl-a oligotrophic regions (monthly climatological Chl-a < 0.1 mg/m^3), (b) Chl-a productive regions, and (c) all regions. (d–f) Same as (a–c), but for the corresponding composites normalized by the local monthly climatological Chl-a. Data are from the 20°–60° latitude band over the study period (October 2023–September 2025).

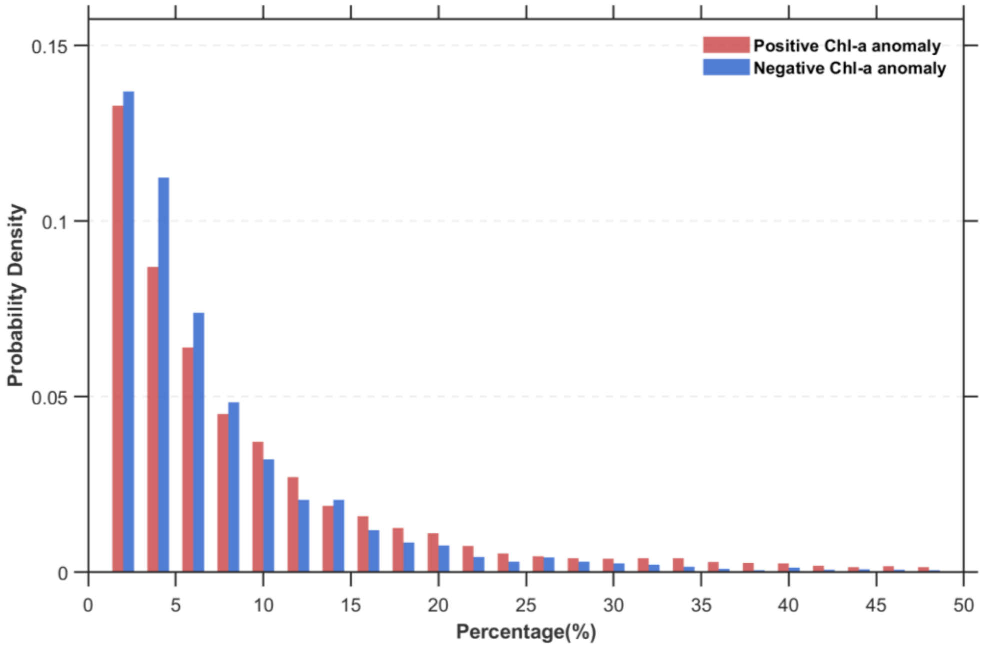

Figure 12. Probability distribution of normalized surface Chl-a anomalies associated with fine-scale eddies. PDF of Chl-a anomalies normalized by local monthly climatology. Red and blue bars denote positive and negative anomalies, respectively. Data are from the 20°–60° latitude band over the study period (October 2023–September 2025).

5. Discussion

5.1. Seasonality Asymmetry in Fine-scale Eddies

Our analysis reveals a marked seasonal cycle in fine-scale eddies, characterized by a sharp winter peak for intensity and frequency—a pattern that stands in stark contrast to mesoscale eddies, which exhibit either no comparable seasonality or a much weaker signal. This observed wintertime enhancement in both the eddy number and amplitude aligns with established theory and numerical simulations [35-38]. A possible mechanism is that under winter conditions, buoyancy loss and intensified wind forcing deepen the mixed layer, which in turn strengthens mixed-layer baroclinicity—a key driver of fine-scale flows that accounts for the pronounced winter peak in intensity and frequency [34].

5.2. Polarity Asymmetry in Fine-scale Eddies

A striking feature of the fine-scale eddy field is its pronounced polarity asymmetry, with CEs both outnumbering and exhibiting stronger amplitudes than AEs. This observed cyclonic dominance is consistent with prior high-resolution simulations and observations that report a systematic bias toward cyclonic vorticity at fine scales [39-41].

The emergence of this asymmetry may be attributed to the combined effects of nonlinear generation and selective dissipation processes inherent to the fine-scale regime. In regions with energetic mesoscale currents, where high strain rates prevail, strain-driven frontogenesis preferentially intensifies density gradients and excites secondary circulations that lead to asymmetric vorticity tendencies, favoring cyclonic vorticity [19].

Concurrently, anticyclonic ageostrophic instability (AAI) acts as a selective filter that preferentially dissipates anticyclonic vorticity. The instability is diagnosed by the criterion:

$$f(A-S) < 0, \quad (4)$$

where $A = f + \zeta$ is the absolute vorticity, ζ is the relative vorticity; $S = \sqrt{^2 + (\partial_x v + \partial_y u)^2}$ is the strain rate. Even when the flow is only modestly anticyclonic, this condition can be satisfied if the strain is sufficiently large, thereby inhibiting the development and persistence of strong AEs [42,43]. While symmetric instability (SI) also contributes to the selective dissipation of AEs, its more restrictive criterion (requiring negative Ertel potential vorticity) makes AAI a more prevalent and efficient mechanism within the turbulent fine-scale field [44].

This pronounced regional contrast in amplitude asymmetry—where the difference is most significant in high-strain, energetic currents like the Gulf Stream (Figures 8d,e)—further supports the proposed mechanisms: the intense strain rates in these regions both enhance strain-driven frontogenesis (favoring cyclonic generation) and lower the threshold for AAI (promoting anticyclonic dissipation), thereby amplifying the polarity asymmetry.

5.3. Limitations

The primary limitation of our eddy detection stems from the fact that SWOT SLA at scales below ~50 km contains significant contributions from unbalanced motions, including internal tides and near-inertial waves [45], which can produce closed contours that mimic eddy-like structures. To mitigate this risk, we use the "filtered" SLA variable, which applies a U-Net–based convolutional neural network to reduce observational noise while preserving balanced signals [25]. Moreover, the detected features collectively exhibit characteristics—persistent closed contours during fast sampling, a pronounced winter peak in activity, and a strong cyclonic polarity dominance—that are not expected from purely wave-like or tidal signals. Two additional lines of evidence reinforce this interpretation. First, although ~32% of eddies fail the temporal persistence criterion, we find they are generally weaker and smaller than validated eddies (Figure 13), and they nonetheless display the same cyclonic-favored amplitude skewness (Figure 14), suggesting that many of these non-validated detections likely correspond to genuine fine-scale eddies, although some may be transient or noisy features. Second, an OW analysis reveals that 75.7% of detected eddies have OW values below $W_0 = -0.2\sigma_w$, consistent with vorticity-dominated coherent structures (Figure 15a). Notably, these OW-identified eddies largely overlap with the high-Ro population: 78.6% of all eddies exhibit Ro > 0.5, reaffirming that the majority correspond to strongly ageostrophic, coherent vortices (Figure 15b). While these diagnostics collectively support the robustness of the census, some misidentification of unbalanced motions may remain, and our results should be interpreted as representing the balanced component of fine-scale eddy variability.

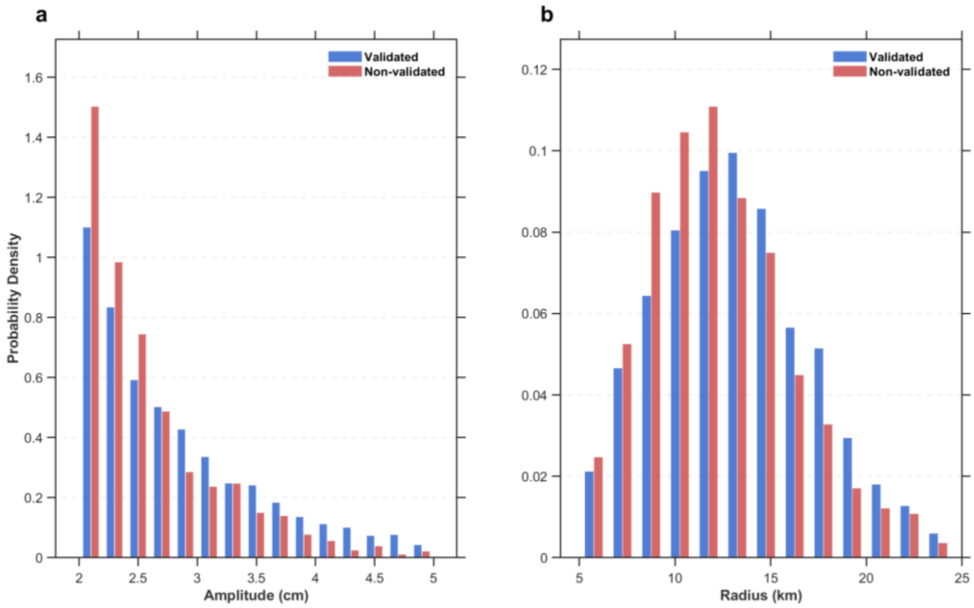

Figure 13. Probability distributions of amplitude and equivalent radius for validated and non-validated fine-scale eddies. PDFs of (a) amplitude and (b) radius for validated and non-validated fine-scale eddies. Blue is for eddies validated by temporal persistence during April to June 2023; red is for non-validated eddies.

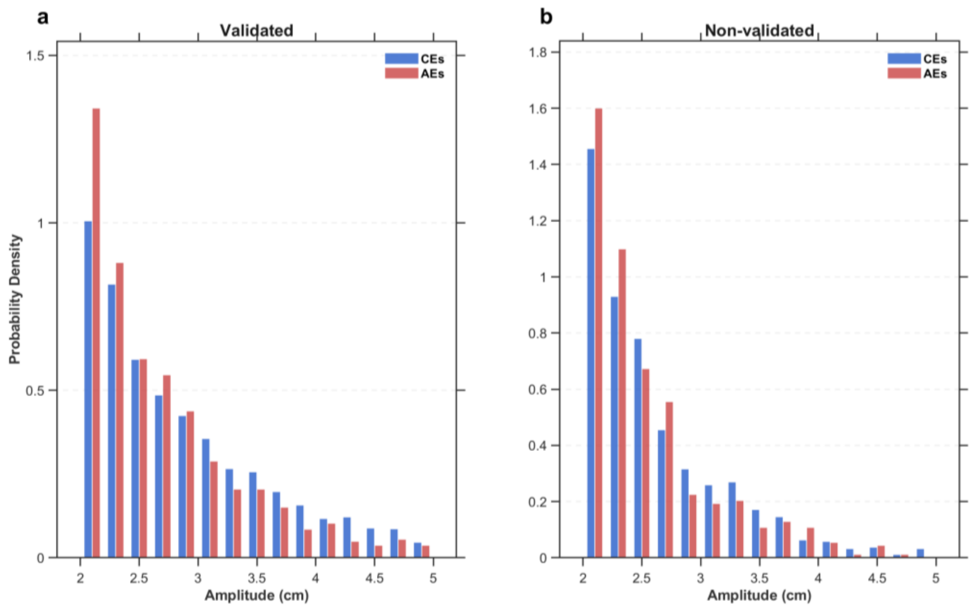

Figure 14. Amplitude distributions of fine-scale eddies by polarity for validated and non-validated eddies. PDFs of amplitude for (a) validated eddies and (b) non-validated eddies. Blue denotes CEs; red denotes AEs.

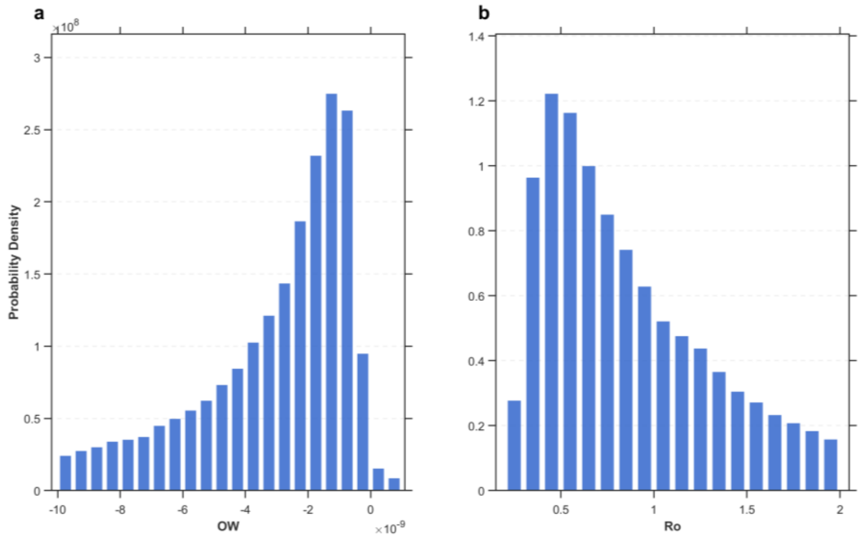

Figure 15. Dynamical diagnostics of fine-scale eddy identifications. PDFs of (a) OW parameter and (b) Ro for the fine-scale eddies.

6. Summary

Utilizing two-dimensional SLA from the SWOT wide-swath altimeter, we present a systematic global census of fine-scale eddies. Our observations reveal that fine-scale eddies are preferentially found in regions of energetic mesoscale currents, including western boundary current extensions, the Antarctic Circumpolar Current, and prominent interior frontal zones. Their activity displays a pronounced seasonal cycle, with a sharp wintertime peak in both intensity and frequency, contrasting with the nearly seasonally invariant mesoscale eddy field. A striking polarity asymmetry is also evident: CEs vastly outnumber and are systematically stronger than AEs, particularly in high-strain regions. Although the chlorophyll-a signature of individual eddies is heterogeneous, a global composite shows a net enhancement of surface chlorophyll-a within eddy cores relative to the surrounding waters. We further acknowledge that SWOT observations at scales below ~50 km contain significant contributions from unbalanced motions, such as internal tides and near-inertial waves; to address this, we use the filtered SLA variable, which employs a U-Net-based convolutional neural network to suppress noise while preserving the balanced signal [25]. The detected features exhibit characteristics—persistent closed contours, a winter activity peak, and strong cyclonic dominance—that are not expected from purely wave-like or tidal signals.

These observations can be interpreted as follows. The winter amplification of fine-scale eddy activity is primarily attributed to mixed-layer deepening driven by enhanced buoyancy loss and wind forcing, which strengthens near-surface baroclinicity and energizes mixed-layer instabilities [34]. The observed cyclonic dominance aligns with theoretical frameworks in which strain-driven frontogenesis preferentially generates cyclonic vorticity [19], while ageostrophic anticyclonic instability (AAI) and symmetric instability (SI) act as selective filters against strong AEs [42–44]. The net increase in surface chlorophyll-a likely stems from a fundamental biogeochemical asymmetry: the ocean's vertical nutrient gradient makes upwelling a far more effective nutrient supply mechanism than downwelling is a dilution process [33], an effect that can be further enhanced by mixed-layer restratification trapping nutrients in the sunlit layer [34]. Nevertheless, some misidentification of unbalanced motions may remain, and our results should be interpreted as representing the balanced component of fine-scale eddy variability.

Author Contributions: Conceptualization, Z.Y. and Z.J.; methodology, Z.Y. and Z.J.; software, Z.Y. and Q.N.; validation, Z.Y.; formal analysis, Z.Y., Z.J., X.Z. and Q.N.; investigation, Z.Y.; resources, Z.J.; data curation, Z.Y.; writing—original draft preparation, Z.Y.; writing—review and editing, Z.Y., Z.J. and X.Z.; visualization, Z.Y.; supervision, Z.J.; project administration, Z.J.; funding acquisition, Z.J. All authors have read and agreed to the published version of the manuscript.

Funding: This study is financially supported by National Key Research and Development Program of China (grant number 2024YFE0114300), and the National Natural Science Foundation of China (42306013 to Z.Y., 92358303 to Z.J.), and Marine S&T Fund of Shandong Province for Laoshan Laboratory (LSKJ202202501 to Z.J.). Q. N. is supported by the National Natural Science Foundation of China (42576009) and the Southern Marine Science and Engineering Guangdong Laboratory (Zhuhai) (SML2023SP207). Computational resources were provided by Laoshan Laboratory (No. LSKJ202300302).

Data Availability Statement: All data used in this study are publicly accessible. The SWOT data can be obtained from https://tds-odatis.aviso.altimetry.fr/thredds/catalog/dataset-l3-swot-karin-nadir-validated/l3_lr_ssh/v2_0_1/Expert/catalog.html. The CMEMS data can be obtained from https://data.marine.copernicus.eu/products. The MODIS data can be obtained from https://oceandata.sci.gsfc.nasa.gov/directdataaccess/. The eddy automatic detection code is public and can be downloaded from https://zenodo.org/records/18399658. The WOA18 data can be obtained from https://www.ncei.noaa.gov/products/world-ocean-atlas.

Conflicts of Interest: The authors declare no conflicts of interest.

References

1. Benitez-Nelson, C.R.; Bidigare, R.R.; Dickey, T.D.; Landry, M.R.; Leonard, C.L.; Brown, S.L.; Nencioli, F.; Rii, Y.M.; Maiti, K.;Becker, J.W.; et al. Mesoscale eddies drive increased silica export in the subtropical Pacific Ocean. Science **2007**, 316, 1017–1021.
2. Chelton, D.B.; Schlax, M.G.; Samelson, R.M.; de Szoeke, R.A. Global observations of large oceanic eddies. Geophys. Res. Lett. **2007**,34, L15606.
3. Chelton, D.B.; Schlax, M.G.; Samelson, R.M. Global observations of nonlinear mesoscale eddies. Prog. Oceanogr. **2011**, 91, 167–216.
4. McGillicuddy, D.J., Jr.; Robinson, A.R.; Siegel, D.A.; Jannasch, H.W.; Johnson, R.; Dickey, T.D.; McNeil, J.; Michaels, A.F.; Knap,A.H. Influence of mesoscale eddies on new production in the Sargasso Sea. Nature **1998**, 394, 263–265 .
5. Zhang, Z.; Wang, W.; Qiu, B. Oceanic mass transport by mesoscale eddies. Science **2014**, 345, 322–324.
6. Ducet, N.; Le Traon, P.Y.; Reverdin, G. Global high-resolution mapping of ocean circulation from TOPEX/Poseidon and ERS-1and -2. J. Geophys. Res. Ocean. **2000**, 105, 19477–19498.
7. LeTraon, P.Y.; Nadal, F.; Ducet, N. An Improved Mapping Method of Multisatellite Altimeter Data. J. Atmos. Ocean. Technol. **1998**,15, 522–533.
8. McWilliams, J.C. Submesoscale Currents in the Ocean. Proc. R. Soc. A. **2016**, 472, 20160117.
9. Duran Gomez, G.S.; Nagai, T. Fine-Scale Eddy Induced Nitrate Upwelling and Effect on Biological Production in the Upstream Kuroshio Current. Sci. Rep. **2025**, 15, 22618.
10. Hewitt, H.; Fox-Kemper, B.; Pearson, B. The small scales of the ocean may hold the key to surprises. Nat. Clim. Change **2022**, 12,496–499.
11. Su, Z.; Wang, J.; Klein, P.; Thompson, A.F.; Menemenlis, D. Ocean submesoscales as a key component of the global heat budget. Nat. Commun. **2018**, 9, 1–8.
12. Zhang, Z.; Liu, Y.; Qiu, B.; Luo, Y.; Cai, W.; Yuan, Q.; Liu, Y.; Zhang, H.; Liu, H.; Miao, M.; et al. Submesoscale inverse energy cascade enhances Southern Ocean eddy heat transport. Nat. Commun. **2023**, 14, 1335.
13. Okubo, A. Horizontal dispersion of floatable particles in the vicinity of velocity singularities such as convergences. Deep Sea Res.Oceanogr. Abstr. **1970**, 17, 445–454.
14. Weiss, J. The dynamics of enstrophy transfer in two-dimensional hydrodynamics. Phys. D Nonlinear Phenom. **1991**, 48, 273–294.
15. Chaigneau, A.; Gizolme, A.; Grados, C. Mesoscale eddies off Peru in altimeter records: Identification algorithms and eddyspatio-temporal patterns. Prog. Oceanogr. **2008**, 79, 106–119.
16. Archer, M.; Wang, J.; Klein, P.; Dibarboure, G.; Fu, L.L. Wide-swath satellite altimetry unveils global submesoscale ocean dynamics. Nature **2025**, 640, 691–696.
17. Fu, L.-L.; Pavelsky, T.; Cretaux, J.-F.; Morrow, R.; Farrar, J.T.; Vaze, P.; Sengenes, P.; Vinogradova-Shiffer, N.; Sylvestre-Baron, A.; Picot, N.; et al. The Surface Water and Ocean Topography Mission: A Breakthrough in Radar Remote Sensing of the Ocean and Land Surface Water. Geophys. Res. Lett. **2024**, 51, e2023GL107652.

18. Du, T.; Jing, Z. Fine-Scale Eddies Detected by SWOT in the Kuroshio Extension. Remote Sens. **2024**, 16, 3488.
19. Qiu, B.; Chen, S. Fine-Scale Upper Ocean Variability in the Kuroshio Extension Region from the Wide-Swath SWOT Measurements. J. Phys. Oceanogr. **2025**, 55, 2229-2242.
20. Cao, L.; Zhang, Y.; Wang, Y.; Hong, M.; Wei, Y.; Qiu, C.; Xia, X. Submesoscale Eddies Identified by SWOT and Their Comparison with Mesoscale Eddies in the Tropical Western Pacific. Remote Sens. **2025**, 17, 3242.
21. Zhang, Z.; Miao, M.; Qiu, B.; Tian, J.; Jing, Z.; Chen, G.; Chen, Z.; Zhao, W. Submesoscale eddies detected by SWOT and moored observations in the Northwestern Pacific. Geophys. Res. Lett. **2024**, 51, e2024GL110000.
22. Zhang, E.; Miao, M.; Zhang, Z. Exploring Submesoscale Processes and Internal Solitary Waves Using SWOT Data in the South China Sea. J. Geophys. Res. Ocean. **2025**, 130, e2025JC022700.
23. Verger-Miralles, E., Mourre, B., Gómez-Navarro, L., Barceló-Llull, B., Casas, B., Cutolo, E., et al. SWOT enhances small-scale eddy detection in the Mediterranean Sea. Geophys. Res. Lett., **2025**, 52, e2025GL116480.
24. Dibarboure, G.; Anadon, C.; Briol, F.; Cadier, E.; Chevrier, R.; Delepoulle, A.; Faugère, Y.; Laloue, A.; Morrow, R.; Picot, N.; et al. Blending 2D topography images from the Surface Water and Ocean Topography (SWOT) mission into the altimeter constellation with the Level-3 multi-mission Data Unification and Altimeter Combination System (DUACS). Ocean Sci. **2025**, 21, 283–323.
25. Tréboutte, A.; Carli, E.; Ballarotta, M.; Carpentier, B.; Faugère, Y.; Dibarboure, G. KaRIn Noise Reduction Using a Convolutional Neural Network for the SWOT Ocean Products. Remote Sens. **2023**, 15, 2183.
26. Ni, Q.; Zhai, X.; Wang, G.; Hughes, C.W. Widespread Mesoscale Dipoles in the Global Ocean. J. Geophys. Res. Ocean. **2020**, 125, e2020JC016479.
27. Souza, J.M.A.C.; de Boyer Montégut, C.; Le Traon, P.Y. Comparison between three implementations of automatic identification algorithms for the quantification and characterization of mesoscale eddies in the South Atlantic Ocean. Ocean Sci. **2011**, 7, 317–334.
28. Dong, J.; Fox-Kemper, B.; Zhang, H.; Dong, C. The seasonality of submesoscale energy production, content, and cascade. Geophys. Res. Lett. **2020**, 47, e2020GL087388.
29. Qiu, B.; Chen, S.; Klein, S.P.; Sasaki, H.; Sasai, Y. Seasonal mesoscale and submesoscale eddy variability along the North Pacific Subtropical Countercurrent. J. Phys. Oceanogr. **2014**, 44, 3079–3098.
30. Yang, P.; Jing, Z.; Sun, B.; Wu, L.; Qiu, B.; Chang, P.; Ramachandran, S. On the upper-ocean vertical eddy heat transport in the Kuroshio extension. Part I: Variability and dynamics. J. Phys. Oceanogr. **2021**, 51, 229–246.
31. Dong, J.; Fox-Kemper, B.; Zhang, H.; Dong, C. The scale of submesoscale baroclinic instability globally. J. Phys. Oceanogr. **2020**, 50, 2649–2667.
32. Ni, Q.; Zhai, X.; Jiang, X.; Chen, D. Abundant Cold Anticyclonic Eddies and Warm Cyclonic Eddies in the Global Ocean. J. Phys. Oceanogr. **2021**, 51, 2793–2806.
33. Mahadevan, A. The impact of submesoscale physics on primary productivity of plankton. Ann. Rev. Mar. Sci. **2016**, 8, 161–184.
34. Boccaletti, G.; Ferrari, R.; Fox-Kemper, B. Mixed Layer Instabilities and Restratification. J. Phys. Oceanogr. **2007**, 37, 2228–2250.
35. Brannigan, L.; Marshall, D.P.; Naveira-Garabato, A.; George Nurser, A.J. The seasonal cycle of submesoscale flows. Ocean Model. **2015**, 92, 69–84.
36. Callies, J.; Ferrari, R.; Klymak, J.M.; Gula, J. Seasonality in submesoscale turbulence. Nat. Commun. **2015**, 6, 6862.
37. Mensa, J.A.; Garraffo, Z.; Griffa, A.; Özgökmen, T.M.; Haza, A.; Veneziani, M. Seasonality of the submesoscale dynamics in the Gulf Stream region. Ocean Dyn. **2013**, 63, 923–941.
38. Rocha, C.B.; Gille, S.T.; Chereskin, T.K.; Menemenlis, D. Seasonality of Submesoscale Dynamics in the Kuroshio Extension. Geophys. Res. Lett. **2016**, 43, 11304–11311.
39. Capet, X.; McWilliams, J.C.; Molemaker, M.J.; Shchepetkin, A.F. Mesoscale to Submesoscale Transition in the California Current System. Part I: Flow Structure, Eddy Flux, and Observational Tests. J. Phys. Oceanogr. **2008**, 38, 29–43.
40. Ohlmann, J.C.; Molemaker, M.J.; Baschek, B.; Holt, B.; Marmorino, G.; Smith, G. Drifter Observations of Submesoscale Flow Kinematics in the Coastal Ocean. Geophys. Res. Lett. **2017**, 44, 330–337.
41. Shcherbina, A.Y.; D’Asaro, E.A.; Lee, C.M.; Klymak, J.M.; Molemaker, M.J.; McWilliams, J.C. Statistics of Vertical Vorticity, Divergence, and Strain in a Developed Submesoscale Turbulence Field. Geophys. Res. Lett. **2013**, 40, 4706–4711.
42. McWilliams, J.C.; Molemaker, M.J.; Yavneh, I. Ageostrophic, Anticyclonic Instability of a Geostrophic, Barotropic Boundary Current. Phys. Fluids **2004**, 16, 3720–3725.
43. Molemaker, M.J.; McWilliams, J.C.; Yavneh, I. Baroclinic Instability and Loss of Balance. J. Phys. Oceanogr. **2005**, 35, 1505–1517.
44. Thomas, L.N.; Taylor, J.R.; Ferrari, R.; Joyce, T.M. Symmetric Instability in the Gulf Stream. Deep Sea Res. Part II **2013**, 91, 96–110.
45. Zhang, X.; Callies, J. Assessing Submesoscale Sea Surface Height Signals from the SWOT Mission. J. Geophys. Res. Ocean. **2025**, 130, e2025JC022879.

Disclaimer/Publisher's Note: The statements, opinions and data contained in all publications are solely those of the individual author(s) and contributor(s) and not of MDPI and/or the editor(s). MDPI and/or the editor(s) disclaim responsibility for any injury to people or property resulting from any ideas, methods, instructions or products referred to in the content.